Individual-Molecule Perspective Analysis of Chemical Reaction Networks: The Case of a Light-Driven Supramolecular Pump

Andrea Sabatino, Emanuele Penocchio, Giulio Ragazzon, Alberto Credi,* and Diego Frezzato*
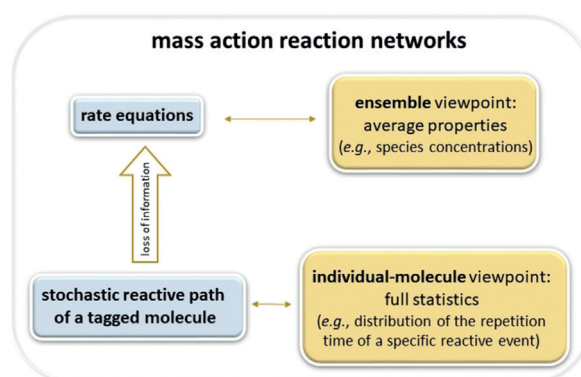
Abstract: *The first study in which stochastic simulations of a two-component molecular machine are performed in the mass-action regime is presented. This system is an autonomous molecular pump consisting of a photoactive axle that creates a directed flow of rings through it by exploiting light energy away from equilibrium. The investigation demonstrates that the pump can operate in two regimes, both experimentally accessible, in which light-driven steps can be rate-determining or not. The number of photons exploited by an individual molecular pump, as well as the precision of cycling and the overall efficiency, critically rely on the operating regime of the machine. This approach provides useful information not only to guide the chemical design of a self-assembling molecular device with desired features, but also to elucidate the effect of the environment on its performance, thus facilitating its experimental investigation.*

Introduction

Living organisms exist away from equilibrium, and so operate naturally occurring molecular machines,[1–3] wherein an energy supply is exploited to drive and sustain specific functions at the nanoscale. Considering the complexity of natural systems, artificial molecular motors[4,5] constitute a platform to gain insights on nonequilibrium systems, although only a few advanced prototypes have been shown to operate away from equilibrium.[4–12] A molecular motor can be rationally described by means of a network of chemical processes[13–16] in which structural transitions are coupled to chemical reactions.[17,18] In suitably engineered systems, the supply of chemicals at a fixed rate (that is, enforcement of chemostats), or the external control on some of the kinetic constants (for example, via photoexcitation), can cause the violation of detailed balance and, ultimately, the emergence of the directed motion at the basis of the function of the machine.[4,5,19,20]

To gain insights on features such as directionality and timing statistics,[21] we shall adopt the perspective of an individual molecule by following its fate along reactive pathways. While the kinetic description at the ensemble level (based on rate equations) is deterministic, the pathway of a tagged molecule is inherently stochastic because the sequence of the reactions involving that molecule, and the times at which such reactions take place, have an aleatory character.[22,23] Clearly, the statistical analysis of a large sample of pathways would provide average quantities in accord with the ensemble view (Scheme 1), but the amount of information that is assessable at the individual-molecule level is much larger.

[*] A. Sabatino, Dr. D. Frezzato
Dipartimento di Scienze Chimiche, Università degli Studi di Padova
Via Marzolo 1, 35131 Padova (Italy)
E-mail: diego.frezzato@unipd.it

E. Penocchio
Complex Systems and Statistical Mechanics, Physics and Materials Science Unit, University of Luxembourg
162 A, avenue de la Faïencerie, 1511 Luxembourg (Luxembourg)

Dr. G. Ragazzon
Department of Chemical and Pharmaceutical Sciences
Università degli Studi di Trieste
via Giorgieri 1,34127 Trieste (Italy)

Prof. Dr. A. Credi
Center for Light Activated Nanostructures (CLAN), Dipartimento di Scienze e Tecnologie Agro-alimentari, Università di Bologna, and Istituto ISOF, Consiglio Nazionale delle Ricerche
Via Gobetti 101, 40129 Bologna (Italy)
E-mail: alberto.credi@unibo.it

Supporting information and the ORCID identification number(s) for the author(s) of this article can be found under:
https://doi.org/10.1002/anie.201908026.

Scheme 1. The individual-molecule approach to mass action chemical kinetics.

Stochastic dynamics of individual molecular rotary motors that undergo structural transitions has been already studied.[21,24] In such cases, the dynamics of the motor is described solely by unimolecular processes. On the other hand, when self-assembly processes are present, the tagged molecular species interacts with a second body in a bimolecular reaction. Such a new component, selected from the environment, then becomes an integral part of the whole system and must be included in the description of its dynamics. In this work we face such a level of complexity which, to the best of our knowledge, has not been considered yet. Indeed, the high significance of non-equilibrium self-assembly in natural[1–3]

and synthetic[25] systems, and in the rapidly growing area of artificial molecular motors,[4,5,19,20] calls for the development of new tools that can enable a deeper mechanistic understanding of these phenomena and, eventually, assist scientists in designing novel devices.

Some of us recently developed a full methodological setup for generating the individual-molecule pathways in the context of mass action chemical kinetics,[26] that is, for high enough concentrations of the chemical species in a thermostatted and well-stirred sample of constant volume (see Computational Methods for an outline). In essence, a pathway of a tagged molecule is generated by means of a Gillespie-like algorithm[27] in which each possible reaction involving that molecule has a propensity to occur. Remarkably, the propensities of multi-molecular processes depend on the composition of the reactive mixture, which thus enters as a regulating factor. This is precisely the case when self-assembly processes are involved.

Herein we apply such a methodology to the case study of a light-powered self-assembling artificial molecular pump, a paradigmatic case in which an external energy source (light) breaks the detailed balancing and originates molecular currents.[6,28,29] The system is described and characterized, from the individual-molecule perspective, in the next sections. Although our analysis is focused on a specific molecular machinery, the presented individual-molecule approach, and the associated methodology for simulating reaction paths, are general and can be employed to inspect the statistical properties of any mass-action-based reaction network.

Results and Discussion

Description of the Reaction Network

The system comprises a macrocyclic polyether, hereafter referred to as the ring, and a molecular axle constituted by a photoswitchable E/Z-azobenzene end (**a**), a cyclopentyl end (**c**), and a central ammonium unit, that acts as recognition site for the ring (Scheme 2, top). The fine chemical tuning of the ring–axle interactions makes it possible to observe, in practice, the self-assembly which otherwise would be strongly disfavored by entropic penalty.[30]

The combination of self-assembly and E/Z isomerization reactions affords the reaction network of Scheme 2 (bottom). The subscripts Δ and $h\nu$ stand for thermal and photo-activated processes, respectively, while superscripts **a** and **c** distinguish the entrance/exit processes at each end of the axle. While the ring and the E-axle preferably associate/dissociate through **a**, upon isomerization to the Z-isomer the ring passes mainly over **c**. Because the isomerization destabilizes the Z-complex, dethreading is thermodynamically favored according to an energy ratchet mechanism.[4,6,31] Moreover, the photoisomerization of the axle is more efficient (higher Z-content at the photostationary state) when the ring is bound, leading to an information ratchet effect.[4,6,31] Taken together, these ratcheting effects provide a kinetic asymmetry[16,32] in the cycle, leading to sustained clockwise cycling under photostationary conditions. The process is associated to
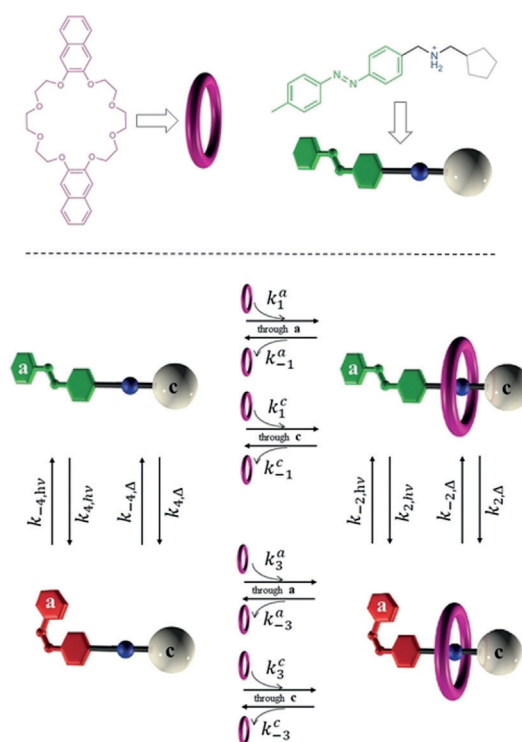
Scheme 2. Top: Molecular components constituting the reaction network and their cartoon representation. Bottom: Investigated kinetic scheme.

directional pumping of axles across a ring or, equivalently, of rings through an axle. Thus, the axle behaves exactly as a photo-activated motor whose function is promoting the directed (on average) flow of rings from the end **a** to the end **c**.

Our focus is on the dynamic behavior of single tagged rings or axles under photo-stationary conditions. In particular, here we investigate some features related with the completion of direct and inverse cycles from the viewpoint of an individual molecule. Let us define the following events:
Ring direct event: the tagged ring enters some axle from the end **a** and then, from here, exits from the end **c** of that axle.
Axle direct event: some ring enters the tagged axle from the end **a** and then, from here, exits from the end **c** of the axle.

Overall, direct events are associated with a unidirectional transit through **a** first, and then **c**. The inverse events describe the opposite directionality and are defined by swapping **a** and **c** in the above definitions. If at the time-zero an event has just occurred, we say that a cycle is completed once the same event takes place again. Note that in between the two events that establish the end points of a directional cycle/event, the reactive history of the tagged ring or of the tagged axle is totally unspecified, that is, multiple threading/dethreading and isomerization reactions can take place.

The system is investigated under conditions that were experimentally tested;[6] namely, total concentrations [axle]$_{tot}$ = 150 μM and [ring]$_{tot}$ = 50 μM in an isothermal and well-stirred reactor (the law of mass action is safely applicable to express the reaction rates), and irradiation at 365 nm. A crucial parameter is the photon flux, $F_{h\nu}$, expressing the rate of the incident photons on the sample. Such a flux, typically

expressed in Einstein s^{-1} (that is, moles of photons per second), can be experimentally controlled and precisely determined by chemical actinometry. In what follows we refer to an irradiated sample of volume 3 mL, and optical path equal to 1 cm (the experimental conditions of Ref. [6]). As briefly reported in the Supporting Information, the kinetic constants of the photo-activated processes are proportional to $F_{h\nu}$. Note that a change of $F_{h\nu}$ indirectly affects the composition at the stationary state. In our investigation, the photon flux is varied by orders of magnitude in a wide range, including the experimental value of 1.67×10^{-9} Einstein s^{-1}.[6] Table 1 collects the adopted values for the kinetic constants (see the Supporting Information for details).

Cycling Times

First, the distributions of the cycling times (Figure 1) are calculated from large numbers of simulated reaction paths of rings and axles (see the Supporting Information for details). Note that without irradiation, the two distributions coincide under the statistical fluctuations. This is in accord with the detailed-balance condition which imposes that direct and inverse events have the same statistical expectation to occur,

Table 1: Values of the kinetic constants employed.[a]

Kinetic constant[b]	Value	Units	Source[c]
$(\rightarrow)k_1^a$	54	L mol^{-1} s^{-1}	(1)
$(\leftarrow)k_{-1}^a$	8.6×10^{-5}	s^{-1}	(1)
k_1^c	0.81	L mol^{-1} s^{-1}	(3)
k_{-1}^c	1.29×10^{-6}	s^{-1}	(2)
k_3^a	0.01	L mol^{-1} s^{-1}	(3)
k_{-3}^a	5.8×10^{-8}	s^{-1}	(2)
$(\leftarrow)k_3^c$	0.81	L mol^{-1} s^{-1}	(1)
$(\rightarrow)k_{-3}^c$	4.7×10^{-6}	s^{-1}	(1)
$(\rightarrow)k_{2,h\nu}$	1.8×10^{-3}	s^{-1}	(1)
$k_{-2,h\nu}$	0.5×10^{-6}	s^{-1}	(1)
$k_{2,\Delta}$	$\approx 10^{-16}$	s^{-1}	(2)
$(\leftarrow)k_{-2,\Delta}$	1.3×10^{-6}	s^{-1}	(1)
$(\leftarrow)k_{4,h\nu}$	1.6×10^{-3}	s^{-1}	(1)
$(\rightarrow)k_{-4,h\nu}$	7.86×10^{-5}	s^{-1}	(1)
$k_{4,\Delta}$	ca. 10^{-15}	s^{-1}	(2)
$k_{-4,\Delta}$	0.14×10^{-6}	s^{-1}	(1)

[a] The signs indicate the fastest processes associated to a clockwise-direct ($\rightarrow$) and counterclockwise-inverse ($\leftarrow$) cycle. [b] Photo-activated processes are referred to the excitation wavelength of 365 nm and to the incident photon flux $F_{h\nu} = 1.67 \times 10^{-9}$ Einstein s^{-1} (experimental conditions of ref. [6]). [c] The labels stand for: (1) experimentally determined, (2) from detailed-balance, (3) likely assumed. See the Supporting Information for details.
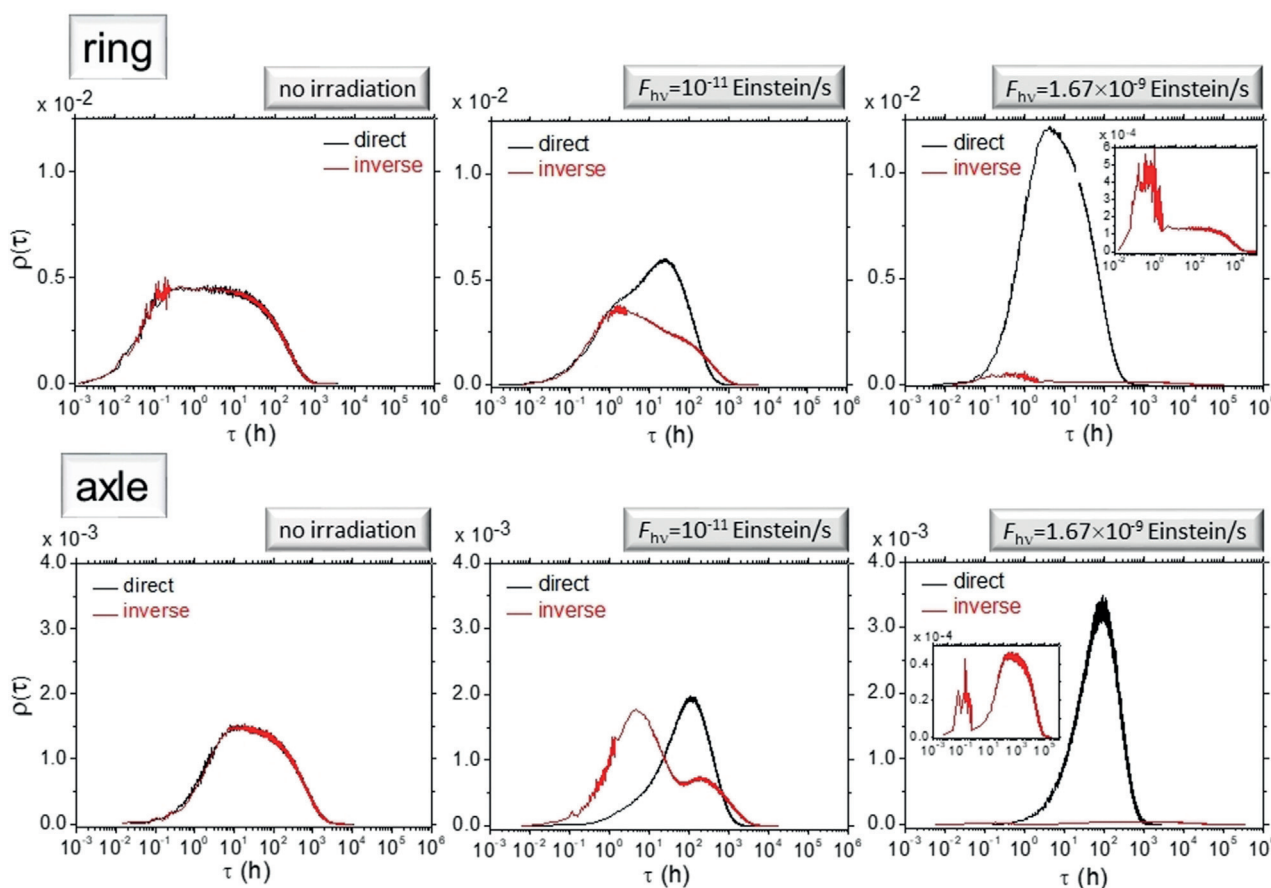

Figure 1. Distributions of the cycling time for the direct cycle (black lines) and the inverse cycle (red lines) from the ring and axle viewpoints. A horizontal logarithmic scale is adopted to magnify the details in the short timescale. Each panel refers to a specific photon flux as indicated. The insets give a blow-up of the flat distributions for the inverse cycles at the large photon flux of the experimental conditions of Ref. [6].

hence any related feature (such as the cycling time) must be statistically equivalent in the two cases. On the contrary, as $F_{h\nu}$ increases, the detailed-balance breakdown affords different distributions for the direct and inverse events. Namely, the distributions for the direct event become narrower, with higher maximum, and shifted toward longer cycling times, whereas the distributions for the inverse event become flatter and lower in magnitude. This behavior lasts until $F_{h\nu}$ reaches the order of 10^{-9} Einstein s^{-1}, when a further increase of the photon flux does no longer affect the shape of the distributions (see the Supporting Information).

Significantly, under the employed experimental conditions ($F_{h\nu} = 1.67 \times 10^{-9}$ Einstein s^{-1}), the directionality is nearly perfect, as indicated by the fact that almost all the performed cycles are direct. The distributions for the inverse events have a complex pattern which displays, at least, a bimodal shape more pronounced as $F_{h\nu}$ increases. This trait can be explained by considering that, when the ring approaches the axle from side **c**, side **a** can be either in E or Z configuration. In the former case inverse dethreading can rapidly happen (first maximum of the distributions), while in the latter some extra time is spent waiting for a photon, being the thermal process ineffective, since k^a_{-3} is very small.

We then assessed the timing and precision of the cycle. To this aim, the average cycling times and the standard deviations were calculated as a function of the photon flux (Figure 2). As expected, for $F_{h\nu}$ equal to zero (values not shown on the logarithmic scale), the average times of direct and inverse cycles do coincide (within 0.8%); namely, the values are 221.8 h for the ring and 667.0 h for the axle. Instead, as $F_{h\nu}$ increases, the time for the direct cycles decreases while the opposite happens for the inverse cycles. The plots clearly demonstrate that the direct cycle becomes more frequent at higher photon flux, whereas the inverse cycle is increasingly impeded. As the photon flux increases, the average times of the direct cycles asymptotically tend to limit values; the same trend can be glimpsed also for the inverse cycles.

The profiles of the standard deviations are found to be very close, or even almost identical, to those of the average values. Such a similarity is not surprising by considering that the distributions of Figure 1, if displayed with a linear horizontal scale, appear very close to exponential distributions (except for a negligible fast initial growth) for which the mean and the standard deviation do coincide. Since the standard deviation quantifies the precision of the cycle timing, we can assert that more intense irradiation increases the precision of the direct cycles while it broadens the distributions of the inverse ones. Importantly, the fact that both the average cycling times and the standard deviations reach a plateau for high values of $F_{h\nu}$ means that at some point delivering more light energy to the system becomes useless for the sake of tuning directionality and precision.

At this stage, a connection between the individual-molecule perspective and the conventional ensemble viewpoint is due. At the stationary state, one can compute the ring macroscopic cycling rate r^{ss}, that is, an ensemble quantity which gives the average net number of ring-along-axle passages, from end **a** to end **c**, per units of time and volume
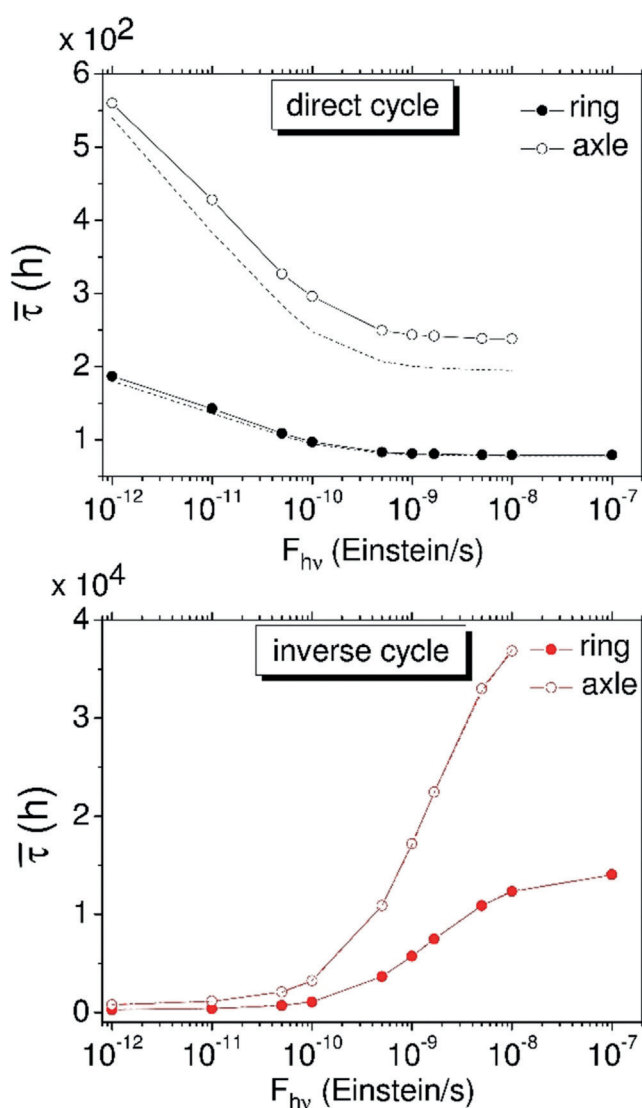

Figure 2. Average direct (top) and inverse (bottom) cycling times and standard deviations, for rings and axle, as a function of the photon flux (for the axle, the data for photon flux 10^{-7} Einstein s^{-1} are not shown because satisfactory statistics could not be reached). Note the use of a different scale on the ordinate axes for direct and inverse cycles. Dashed lines represent the standard deviations (for the inverse cycles, they are essentially coincident with the average cycling times).

under stationary conditions. The profile of r^{ss} is shown in Figure 3 for a broad range of values of the photon flux. In the absence of irradiation, $r^{ss} = 0$ (no directionality can be present under detailed-balanced conditions); then the curve rises as $F_{h\nu}$ increases until a plateau is reached. The value of r^{ss} and the average cycling times of the ring are related by [Eq. (1)]:

$$r^{ss} = [\text{ring}]_{\text{tot}} (\bar{\tau}^{-1}_{\text{direct}} - \bar{\tau}^{-1}_{\text{inverse}}) \tag{1}$$

where $[\text{ring}]_{\text{tot}}$ is the total ring concentration (50 µM in the present case). A similar relation can be also written in terms of $[\text{axle}]_{\text{tot}}$ and of the cycling times of the axle. As displayed in the inset of Figure 3, the linear regression of $\bar{\tau}^{-1}_{\text{direct}} - \bar{\tau}^{-1}_{\text{inverse}}$ versus r^{ss} shows a perfect fit with slope $1/[\text{ring}]_{\text{tot}}$. Equation (1) provides the interpretation of r^{ss} in terms of kinetic informa-
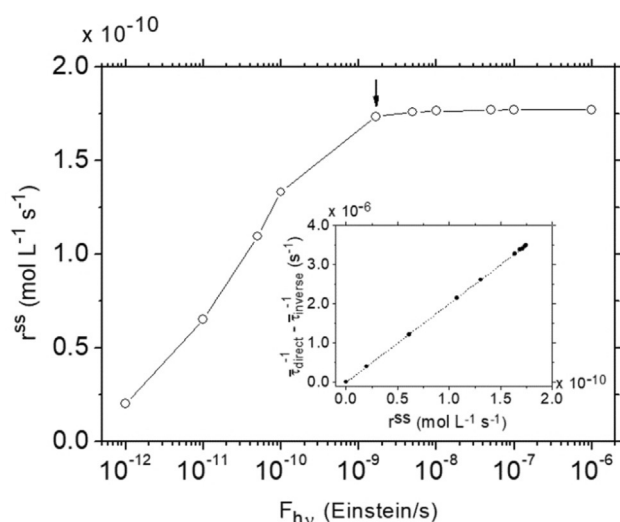
Figure 3. Macroscopic cycling rate of the ring, r^{ss} (average net number of ring-along-axle passages per units of time and volume at the stationary state) as a function of the photon flux. The arrow indicates the experimental conditions of Ref.[6]. The inset shows the linear relation between $\bar{\tau}_{direct}^{-1} - \bar{\tau}_{inverse}^{-1}$ (individual molecule viewpoint) and r^{ss} (ensemble viewpoint) with slope 1/[ring]$_{tot}$.

Figure 4. Distributions of the number of photo-isomerizations of the axle, in its direct cycle, for different values of the photon flux.

tion at the individual-molecule (individual ring) level. For $\bar{\tau}_{direct}^{-1} = \bar{\tau}_{inverse}^{-1}$, that is, for detailed-balanced network in the absence of irradiation, $r^{ss} = 0$ is correctly obtained; for $\bar{\tau}_{inverse}^{-1} > \bar{\tau}_{direct}^{-1}$, as it happens under photo-stationary conditions with the present parametrization of the reaction scheme, $r^{ss} > 0$, corresponding to an average net flow of rings from the ends **a** to **c** of the axles. It is worth stressing that while r^{ss} is simply related to the deterministic average net current of rings, the distributions of the cycling times give much more information, for example about the precision of the cycles or the pumping mechanism.

Two different working regimes clearly emerge from the behavior of r^{ss}: 1) small photon fluxes, in which F_{hv} is a rate-determining parameter; and 2) large photon fluxes, in which the cycling rate is no longer affected by changes in F_{hv}. Our results indicate that values of F_{hv} close to 10^{-9} Einstein s^{-1} correspond to an optimal working condition, which maximizes both directionality and precision of the pump by dissipating the minimum amount of energy. As highlighted by the arrow in Figure 3, it turns out that the flux employed in the experiments[6] falls within the optimal range.

Photoisomerizations

Let us focus now on an individual axle. We first consider the number of photo-induced isomerizations during the completion of a direct cycle, the distribution of which for different photon fluxes is shown in Figure 4. Note that an even–odd alternation develops and becomes increasingly pronounced as F_{hv} increases. In particular, even numbers of photo-isomerizations per cycle are more likely than odd numbers. Such a behavior can be rationalized as follows. Once the cycle is completed, the axle is likely in the Z configuration. To accommodate the next ring, that particular axle has to
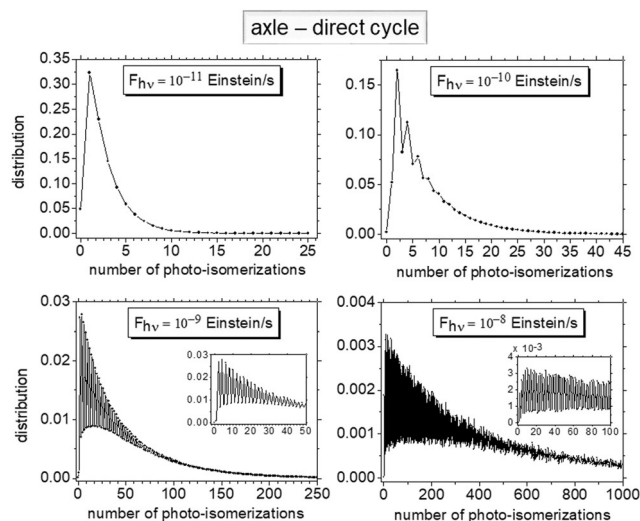
undergo an odd number of isomerizations so that a ring can pass over the end **a** of the axle in E configuration. Successively, a further odd number of isomerizations must take place to bring the axle in the Z configuration, so that the ring can exit from the end **c** and complete the cycle. The total number of photo-isomerizations to complete a cycle is thus strongly biased toward even values. When F_{hv} is very small, thermal isomerization is significant, and the distinction between even and odd values is negligible for the sole photo-induced processes. As F_{hv} increases, the photo-induced processes become predominant and the even–odd pattern emerges (as is evident from the sequence in Figure 4).

It is worth noting that the distributions peak around 2–4 photons per cycle until F_{hv} is increased up to 10^{-9} Einstein s^{-1}. This means that the pump works efficiently (that is, the relative majority of cycles is completed using such minimum number of photons) in the regime where the photon flux is rate-determining. Above the threshold photon flux, the system can no longer effectively process photons arriving with such a high rate, and more photons are used while a cycle is completed.

Again from the viewpoint of an individual axle, for each number of photo-isomerizations we have identified the minimum cycling time within the sample of simulated direct cycles (see the Supporting Information). It emerges that, for a given number of photo-isomerizations to occur, the cycling time (both for the direct and inverse cycle) cannot drop below a minimum threshold. This means that making a cycle with a given number of photo-isomerizations requires a minimum time.

Exploring Different Experimental Conditions

In the conditions considered above, the excitation wavelength of 365 nm corresponds to molar absorption coefficients of the axle in the E and Z forms, with and without the ring, that are sensibly different one from the other. Such a differ-

ence is likely at the basis of an information ratchet effect, which adds to the asymmetry arising from the different stability of the *E* and *Z* complexes (energy ratchet). These two contributions to the overall asymmetry ultimately manifest in the bias toward direct cycles, as shown in Figure 3. With a basic model for the photo-excitation kinetic constants at hand (see the Supporting Information), the analysis can be performed for different excitation wavelengths. We therefore envisioned to investigate the properties of the system while stimulated at 436 nm. At this experimentally accessible wavelength, the molar absorption coefficients for the axle are not affected by the presence of the ring. Indeed, while all thermal kinetic constants in Table 1 remain unchanged, the photo-activated contributions are closer to each other (for instance, at the photon flux of 10^{-9} Einstein s^{-1} the values are $k_{2,hv} \simeq k_{4,hv} = 1.6 \times 10^{-4}$ s^{-1} and $k_{-2,hv} \simeq k_{-4,hv} = 8.5 \times 10^{-4}$ s^{-1}; see the Supporting Information for more details). Therefore, the information ratchet component of the asymmetry vanishes. Under these irradiation conditions the whole asymmetry arises from the thermodynamic stability of the *E* and *Z* complexes. Figure 5 (compare with Figure 2) shows the
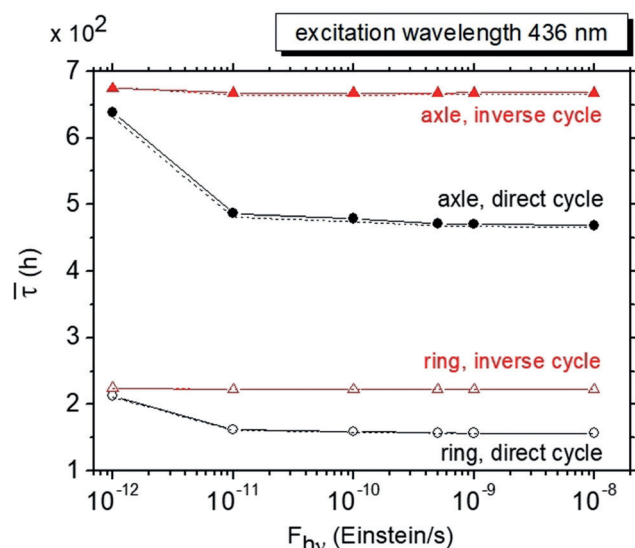

Figure 5. Average cycling times (symbols) and standard deviations (dashed lines), for rings and axles, as a function of the photon flux at the excitation wavelength 436 nm.

average cycling times and the standard deviations for the direct and inverse cycles of rings and axles when the excitation wavelength is 436 nm. Furthermore, examples of distribution of the cycling times at this wavelength (to be compared with those in Figure 1) are given in the Supporting Information.

As a whole, it emerges that at 436 nm the direct cycles are still privileged, but the cycling asymmetry direct-versus-inverse is strongly reduced and the standard deviations are higher, thus implying a smaller precision. This observation highlights the crucial contribution of information ratchet to the operation of the present molecular machinery. Moreover, it is observed that the optimal photon flux is two orders of

magnitude lower than that required for the 365 nm irradiation (10^{-11} vs. 10^{-9} Einstein s^{-1}). This implies that the thermal reactions become rate-determining at lower photon fluxes, likely because of the higher rate constants associated to the *Z* to *E* photoisomerizations, favoring the slowest photochemical step of the direct cycle. Overall, operating the system at 436 nm requires the use of a lower photon flux to reach the optimal working conditions albeit providing a lower degree of asymmetry.

Similarly, one could inspect how the cycling properties are affected by changes of temperature, solvent, and concentration. The solvent effect, in particular, can be guessed under the assumptions that 1) the solvent merely acts as an inert viscous medium in which the reactions take place, and 2) the photo-excitation constants depend weakly on the solvent properties. These conditions could be verified when solvents with similar chemical properties are compared. In such a case, the thermal kinetic constants of all unimolecular processes (including thermal Z to *E* conversions) are roughly inversely proportional to the medium viscosity, η_{solv}, according to Kramers' theory of reactive processes activated by thermal fluctuations in the overdamped regime.[33] Also for the bimolecular processes (threading–dethreading of the rings), the thermal kinetic constants are expected to be inversely proportional to the viscosity according to a stochastic description of the reactant dynamics.[34] By taking into account that the rates of the photo-activated processes are proportional to F_{hv}, it follows that all kinetic constants (of both thermal and photo-activated channels) would be enhanced or decreased by the same factor if the product $F_{hv} \times \eta_{solv}$ is kept fixed. This implies that the composition at the stationary state would remain fixed, and that all inspected dynamical features simply appear speeded or slowed down in the same way. In particular, the degree of asymmetry between inverse and direct cycles should remain nearly constant at fixed $F_{hv} \times \eta_{solv}$. In practice, this means that in a more viscous solvent, the same degree of cycling asymmetry should be achieved with lower light intensity. Under these conditions the timescale of both direct and inverse cycles are expected to increase, since all kinetic constants would be smaller. On the contrary, moving to a less viscous solvent and increasing the photon flux, the timescale of cycling is expected to decrease. Overall, under the indicated assumptions it should be possible to modulate the timing of cycling without affecting the overall asymmetry. Extension of such predictions to solvents with significantly different chemical properties should be validated experimentally or by means of a sound modelling of the solvent effect.

Conclusion

In summary, we applied a novel methodology for inspecting mass action chemical reaction networks under the point of view of individual tagged molecules. In particular, the method has been employed to gain unprecedented (and previously inaccessible) insight on the first autonomous artificial supramolecular pump. This is a paradigmatic case in which light breaks the detailed balance and originates molecular currents,

thereby driving a self-assembling system away from equilibrium.[6] We have demonstrated that the distribution of cycling times has an apparent bimodal shape, and that there is a higher likelihood to complete a cycle by processing an even number of photons. While it was previously observed that light-induced processes can be rate-determining under practical operational conditions of a molecular rotary motor,[21] here we have shown the direct consequences on the fate of individual molecules: when the light-driven step is rate-determining, the relative majority of switches use only two or four photons to perform a complete cycle, whereas under saturating conditions more photons are used. The precision of cycling, which can be disclosed solely from an individual-molecule perspective, improves only up to the saturating regime, thus defining the optimal working conditions of the molecular motor. Remarkably, the present investigation indicates that in light-driven systems based on photoswitches the directionality arises from preventing the unwanted pathways, rather than promoting the desired ones, as it occurs in chemically-driven systems.[35]

The employed methodology,[26] which is versatile and applicable to any molecular system whose functioning can be framed as a chemical reaction network, can be used to establish how the relevant features of a synthetic machine (for example, average time and precision of a cycle) depend on the intrinsic kinetic constants and on externally tunable parameters (for example, the intensity and wavelength of the irradiation in the case studied here). Furthermore, while here we focused on stationary conditions, individual-molecule paths could be generated also in transient conditions during which the system composition changes. This approach can be greatly helpful for the rational design and optimal operation of dynamic stimuli-responsive chemical systems to function as molecular devices and machines.

Computational methods

We outline here only on the strategy for generating individual-molecule reaction paths at the stationary state. Details on the employed rate equations solver, and about the composition at the photo-stationary state, are provided in the Supporting Information.

The individual-molecule reaction paths at the stationary state have been simulated by means of a Gillespie-like stochastic simulation algorithm algorithm[27] fully described in Ref. [26]. Here we give only an outline. In general terms, let j be the species index, and s_j be an index that specifies a molecular site (or state) of the tagged molecular moiety in a molecule of species j. Then, let m be the index that labels the elementary reactions. At the stationary state, the rate of the reaction m is expressed by

$$r_m^{ss} = k_m \prod_j [j]_{ss}^{\nu_{R_j}^{(m)}}$$

where $\nu_{R_j}^{(m)}$ is the stoichiometric coefficient of the species j as reactant in the reaction m. Finally, let $\rho_{\text{transf}}^{ss}(s_i, m, \tau_r | s_j)\delta\tau_r$ be the probability that, if the moiety is currently in the state s_j, it will be transferred to the state s_i by means of the reaction m between τ_r and $\tau_r + \delta\tau_r$. With the above positions, in Ref. [26] it has been proved that

$$\rho_{\text{transf}}^{ss}(s_i, m, \tau_r | s_j) = p_{j,R_m}^{ss} \, \phi_m(s_i | s_j)\exp(-\tau_r \alpha_j),$$

where

$$p_{j,R_m}^{ss} = \nu_{R_j}^{(m)} \, \frac{r_m^{ss}}{[j]_{ss}}$$

is such that $p_{j,R_m}^{ss} \delta\tau_r$ gives the probability that the tagged molecule of species j (that is, the one carrying the tagged moiety) will participate as reactant in the reaction m in the next time-interval $\delta\tau_r$; then, $\phi_m(s_i | s_j)$ is the probability a priori that the reaction m brings the moiety into the state s_i (in a molecule of species i) starting from the state s_j (in a molecule of species j); finally, the rate $\alpha_j = \sum_m p_{j,R_m}^{ss}$ gives the total propensity of the molecule of species j to react under stationary conditions. Given the actual state of the moiety, the time τ_r of its next jump, the reaction m that will occur, and the arrival state s_i (possibly equivalent to the starting one) are randomly drawn from the distribution $\rho_{\text{transf}}^{ss}(s_i, m, \tau_r | s_j)$. The state of the moiety is then updated and the time is shifted by τ_r. The iteration of such steps generates a reaction path. In the context of this work, the moiety corresponds to a ring or to an axle. In each case, the reactive path is continued up to accumulate a prescribed number of cycles that ensures the required quality of statistics in the post-production analysis. The photon flux values, and the corresponding numbers of cycles that have been generated, are provided in the Supporting Information. All distributions of the cycling times have been obtained by means of a standard histogram construction with binning in the logarithmic scale.

Acknowledgements

Conflict of interest

The authors declare no conflict of interest.

[1] S. Mann, *Angew. Chem. Int. Ed.* **2008**, *47*, 5306–5320; *Angew. Chem.* **2008**, *120*, 5386–5401.
[2] P. M. Hoffmann, *Life's Ratchet: How Molecular Machines Extract Order from Chaos*, Basic Books, New York, **2012**.
[3] R. D. Astumian, *Biophys. J.* **2010**, *98*, 2401–2409.
[4] S. Kassem, T. van Leeuwen, A. S. Lubbe, M. R. Wilson, B. L. Feringa, D. A. Leigh, *Chem. Soc. Rev.* **2017**, *46*, 2592–2621.
[5] S. Erbas-Cakmak, D. A. Leigh, C. T. McTernan, A. L. Nussbaumer, *Chem. Rev.* **2015**, *115*, 10081–10206.
[6] G. Ragazzon, M. Baroncini, S. Silvi, M. Venturi, A. Credi, *Nat. Nanotechnol.* **2015**, *10*, 70–75.
[7] N. Koumura, R. W. J. Zijlstra, R. A. van Delden, N. Harada, B. L. Feringa, *Nature* **1999**, *401*, 152–155.
[8] M. R. Wilson, J. Solá, A. Carlone, S. M. Goldup, N. Lebrasseur, D. A. Leigh, *Nature* **2016**, *534*, 235–240.
[9] C. Cheng, P. R. McGonigal, S. T. Schneebeli, H. Li, N. A. Vermeulen, C. Ke, J. F. Stoddart, *Nat. Nanotechnol.* **2015**, *10*, 547–553.

[10] S. Erbas-Cakmak, S. D. P. Fielden, U. Karaca, D. A. Leigh, C. T. McTernan, D. J. Tetlow, M. R. Wilson, *Science* **2017**, *358*, 340–343.

[11] L. Greb, J.-M. Lehn, *J. Am. Chem. Soc.* **2014**, *136*, 13114–13117.

[12] V. Serreli, C.-F. Lee, E. R. Kay, D. A. Leigh, *Nature* **2007**, *445*, 523–527.

[13] E. Mattia, S. Otto, *Nat. Nanotechnol.* **2015**, *10*, 111–119.

[14] O. S. Miljanić, *Chem* **2017**, *2*, 502–524.

[15] G. Ashkenasy, T. M. Hermans, S. Otto, A. F. Taylor, *Chem. Soc. Rev.* **2017**, *46*, 2543–2554.

[16] G. Ragazzon, L. Prins, *Nat. Nanotechnol.* **2018**, *13*, 882–889.

[17] A. B. Kolomeisky, M. E. Fisher, *Annu. Rev. Phys. Chem.* **2007**, *58*, 675–695.

[18] C. Bustamante, D. Keller, G. Oster, *Acc. Chem. Res.* **2001**, *34*, 412–420.

[19] A. Coskun, M. Banaszak, R. D. Astumian, J. F. Stoddart, B. A. Grzybowsky, *Chem. Soc. Rev.* **2012**, *41*, 19–30.

[20] C. Pezzato, C. Cheng, J. F. Stoddart, R. D. Astumian, *Chem. Soc. Rev.* **2017**, *46*, 5491–5507.

[21] E. M. Geertsema, S. J. van der Molen, M. Martens, B. L. Feringa, *Proc. Natl. Acad. Sci. USA* **2009**, *106*, 16919–16924.

[22] a) J. R. Moffitt, Y. R. Chemla, C. Bustamante, *Methods Enzymol.* **2010**, *475*, 221–257; b) J. R. Moffitt, C. Bustamante, *FEBS J.* **2014**, *281*, 498517.

[23] a) S. Bai, D. Zhou, M. J. Davis, R. T. Skodje, *J. Phys. Chem. Lett.* **2015**, *6*, 183–188; b) S. Bai, R. T. Skodje, *J. Phys. Chem. Lett.* **2017**, *8*, 3826–3833.

[24] L. Moro, M. di Gioia, M. Calvaresi, E. Bakalis, F. Zerbetto, *ChemPhysChem* **2014**, *15*, 1834–1840.

[25] C. R. Benson, C. Maffeo, E. M. Fatila, Y. Liu, E. G. Sheetz, A. Aksimentiev, A. Singharoy, A. H. Flood, *Proc. Natl. Acad. Sci. USA* **2018**, *115*, 9391–9396.

[26] A. Sabatino, D. Frezzato, *J. Chem. Phys.* **2019**, *150*, 134104.

[27] a) D. T. Gillespie, *J. Phys. Chem.* **1977**, *81*, 2340–2361; b) D. T. Gillespie, A. Hellander, L. R. Petzold, *J. Chem. Phys.* **2013**, *138*, 170901.

[28] G. Ragazzon, M. Baroncini, S. Silvi, M. Venturi, A. Credi, *Beilstein J. Nanotechnol.* **2015**, *6*, 2096–2104.

[29] E. Sevick, *Nat. Nanotechnol.* **2015**, *10*, 18–19.

[30] E. M. Sevick, D. R. M. Williams, *Nano Lett.* **2016**, *16*, 671–674.

[31] R. D. Astumian, *Phys. Chem. Chem. Phys.* **2007**, *9*, 5067–5083.

[32] R. D. Astumian, *Chem. Commun.* **2018**, *54*, 427–444.

[33] R. Zwanzig, *Nonequilibrium statistical mechanics*, Oxford University Press, New York, **2001**.

[34] G. J. Moro, M. G. Severin, *J. Chem. Phys.* **2001**, *114*, 4565–4578.

[35] R. D. Astumian, *Biophys. J.* **2015**, *108*, 291–230.